STRUCTURAL CONTROL AND HEALTH MONITORING
Struct. Control Health Monit. 2012; **19**:650–671
Published online 24 May 2011 in Wiley Online Library (wileyonlinelibrary.com). DOI: 10.1002/stc.461

Correlative sensor array and its applications to identification of damage in plate-like structures

Long Yu[1,2], Li Cheng[1] and Zhongqing Su[1,*,†,‡]

[1]*Department of Mechanical Engineering, The Hong Kong Polytechnic University, Kowloon, Hong Kong SAR*
[2]*School of Mechanics, Civil Engineering and Architecture, Northwestern Polytechnical University, 710072, Xi'an, China*

SUMMARY

Lamb waves, the guided elastic waves in thin plate/shell structures, have been the core of intensive research for developing cost-effective damage identification techniques over decades. In this regard, appropriate and optimal allocation of actuators and sensors in a sensor array/network is a pivotal concern for achieving sufficient information to describe the damage and meanwhile for minimising interferences of multiple wave modes and complex wave reflection from structural boundaries. An active sensor array comprising a number of miniaturised piezoelectric wafers aligned strategically was developed in the study, named *correlative sensor array* (CSA) to reflect its mechanism based on signal correlation processing. Using the time differences of different Lamb waves captured by individual array members, a CSA is able to facilitate awareness of structural damage and subsequently to locate it. To ascertain time difference accurately, a signal processing algorithm capitalising on signal correlation and moving-window-based likelihood searching was integrated with the array. The CSA with integrated signal processing algorithm was then numerically and experimentally applied to the identification of a through-thickness hole in an aluminium plate, and the identification results have shown the feasibility and effectiveness of the CSA for pinpointing damage in plate-like structures. As supplement, limitations of CSA-based damage detection in terms of the effective detection area and sensitivity were explored.

Received 16 September 2010; Revised 28 March 2011; Accepted 6 April 2011

KEY WORDS: correlative sensor array (CSA); Lamb waves; damage identification; time difference; signal correlation; moving-window-based likelihood searching (MWLS)

1. INTRODUCTION

Guided elastic waves and in particular Lamb waves (Lamb waves are the modality of elastic waves in a thin plate-/shell-like structure with planar dimensions being far greater than that of the thickness and with the wavelength being in the order of the plate/shell thickness) have been intensively examined as a promising candidate to develop cost-effective damage identification techniques [1–12]. Their superb capabilities for damage identification include low attenuation, strong penetration, convenience of activation and acquisition, low energy consumption and, most importantly, high sensitivity to structural damage and material inhomogeneities even when they are small in size or lie beneath the structural surface.

When practically implementing guided-wave-based damage identification, a single sensor, performing local acquisition of waves, can hardly provide sufficient information for describing the damage, eroding the confidence in accepting identification results. A multitude of spatially distributed sensors are often networked to configure a sensor array/network. By 'communicating' with each other, a sensor array/network certainly provides added information, increased redundancy and enhanced reliability of signal acquisition. To form a

*Correspondence to: Zhongqing Su, Department of Mechanical Engineering, The Hong Kong Polytechnic University, Kowloon, Hong Kong SAR.
†Email: MMSU@polyu.edu.hk
‡Asst. Prof.

sensor array/network, one can employ a large number of sensors to form a very dense configuration with the spacing between two sensors similar to or smaller than the scale of anticipated damage, consistent with the biologically inspired nervous systems including those of human beings. However, such a dense sensor network is obviously impractical in engineering applications. A realistic solution is the use of sparse configurations consisting of a small number of sensors, with the sensor spacing far greater than the scale of the anticipated damage, which is the common case in practice [13,14]. In this regard, appropriate and optimal allocation of actuators/sensors plays a pivotal role in achieving sufficient information and meanwhile minimising interferences of multiple wave modes and complex wave reflection from structural boundaries.

In this study, following a comparison of various collocation schemes for sensors in a sensor array/network that are prevalently adopted for guided-wave-based damage identification, an active sensor array approach was developed, which was named *correlative sensor array* (CSA) to address its mechanism. Comprising a number of miniaturised piezoelectric wafers aligned strategically, a CSA explores the time differences of different Lamb waves scattered by structural damage and then captured by individual sensors in the array. To ascertain time difference accurately, an integrated processing algorithm capitalising on signal correlation and moving-window-based likelihood searching (MWLS) was introduced. With ascertained time difference, the wave scattering source (i.e. damage) can be triangulated accordingly. To demonstrate the feasibility and effectiveness of the CSA-based damage identification strategy, numerical simulation and experimental validation were carried out, in which the CSA and integrated signal processing algorithm were employed to locate a through-thickness hole in an aluminium plate.

2. SENSOR ARRAY/NETWORK FOR GUIDED-WAVE-BASED DAMAGE IDENTIFICATION

For the purpose of identifying structural damage based on guided waves, allocation of transducers (*actuator* and *sensor* constituting the generic term *transducer*) in a sensor array/network can be diverse, exemplified by some representatives shown in Figure 1 [15,16]. In whichever scheme, transducers must be placed appropriately, so as to achieve (i) the minimum number of transducers required but not at the cost of sacrificing adequate information to describe the damage and losing tolerance to measurement noise and uncertainties and (ii) the sufficient sensitivity to damage-scattered waves which contain the information pertaining to damage. The preceding two requirements have raised the concerns about the optimisation of a sensor array/network [17–19] in terms of sensor number and location, respectively. Through optimisation, a compromise between network coverage (damage-detectable area) and sensitivity with regard to damage can be achieved. In this aspect, some basic considerations are: (i) sensors and actuators should be positioned appropriately relative to structural boundaries to avoid influence of boundary-reflected waves on those scattered by damage; (ii) sensors should be positioned not too far away from the region where damage might exist to be sensitive to damage-scattered waves; (iii) the distance between actuators and sensors should not be too large to insure that waves would not be attenuated considerably before being received; (iv) the sensor network should possess a certain degree of robustness to maintain reliability if some sensors malfunction; and (v) transducers should be small in size and inexpensive, e.g. piezoelectric lead zirconate titanate (PZT) elements, so that they can easily be attached to a structure and deployed in a large number. Following intensive research, some sensor network techniques have been commercialised, represented by the SMART Layer® (manufactured by Acellent Technologies, Inc., Sunnyvale, CA 94085, USA) [13,20,21] and HELP Layer® (manufactured by the French Aerospace Lab, France) [22].

Although there is no clear demarcation, allocation of sensors in a sensor array/network can fall into one of the following two schemes in conformity to the orientation along which the incident diagnostic waves access into the inspection area (in what follows the *inspection area* is referred to as the region within which the damage can be detected):

2.1. Inwards accessing scheme

Exemplified by the scenarios shown in Figure 1(a) and (b), actuators and sensors are located near the fringes of the inspection area. The incident diagnostic waves are activated by actuators to propagate

DOI: 10.1002/stc

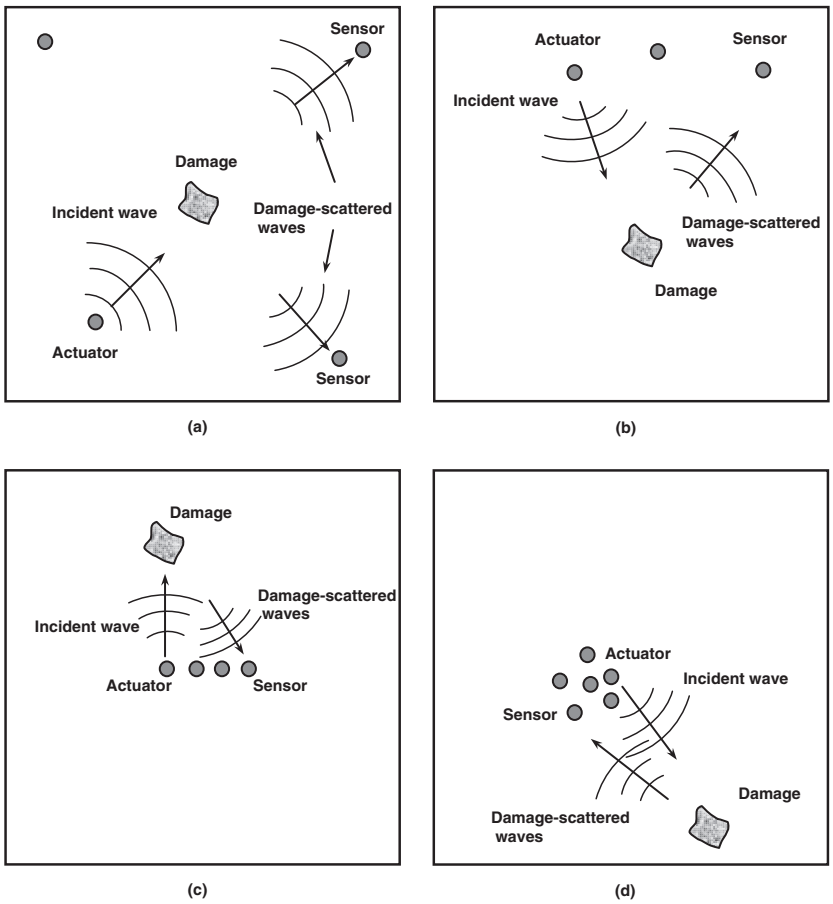

Figure 1. Representative allocation schemes for transducers in a sensor array/network that are widely adopted for guided-wave-based damage identification [15,16]. (a) inwards accessing scheme I; (b) inwards accessing scheme II; (c) outwards accessing scheme I; and (d) outwards accessing scheme II.

inwards to access the inspection area, scattered by damage, if any, and then captured by sensors. With ascertained difference between time-of-flights (ToFs; ToF is defined as the time consumed for a wave to travel a certain distance) of the damage-scattered and incident diagnostic waves (as illustrated in Figure 2) in signals captured via at least two actuator–sensor paths, damage can in principle be triangulated. The detailed description of ToF-based damage triangulation can be referred to elsewhere [12].

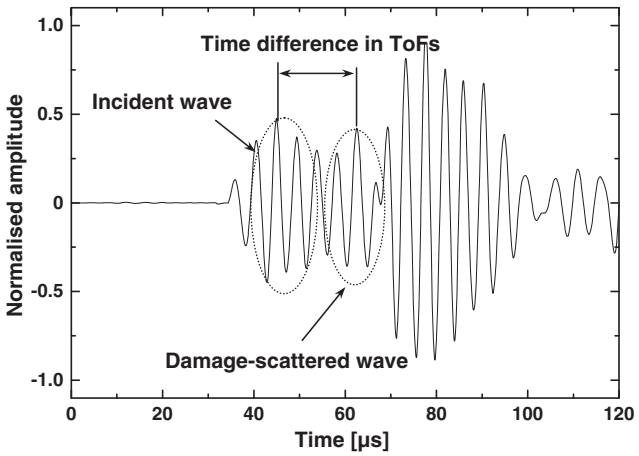

Figure 2. Definition of difference in ToFs between the incident diagnostic wave and damage-scattered wave.

DOI: 10.1002/stc

2.2. Outwards accessing scheme

Exemplified by the scenarios shown in Figure 1(c) and (d), actuators and sensors are centralised approximately within the inspection area. The incident diagnostic waves are activated by actuators to propagate outwards to access the inspection area, echoed back by damage, if any, and then captured by sensors. With ascertained difference between ToFs of the damage-scattered waves in signals captured by at least two sensors, damage can in principle be triangulated, as detailed elsewhere [12], whereas rationale of such a means for locating damage can be traced back to earlier publication [5].

The most prominent advantage of the outwards accessing scheme over the other lies on the fact that in such a scheme the incident diagnostic waves often encounter damage earlier than structural boundaries, and as a consequence the damage-scattered waves are observed first in a captured signal with reduced possibility to be masked by boundary reflections, benefiting signal interpretation. *Phased-array beamforming* is a typical outwards accessing scheme, which can widely be found in applications including sonar tracking, medical imagery, seismology and oceanography because in these applications it is almost impossible to allocate actuators/sensors at fringes of an inspection area and launch signals to propagate inwards to access the inspection area. Phased-array beamforming has been introduced to guided-wave-based damage identification [6,23–27], and *piezoelectric wafer active sensors* (PWAS) technique is amongst those with demonstrated effectiveness. PWAS employs a number of piezoelectric wafers, positioned along a straight line to form a sensor array, as the example shown in Figure 3 [23]. Piezoelectric wafers in a PWAS, called *array elements*, are individually and sequentially activated with

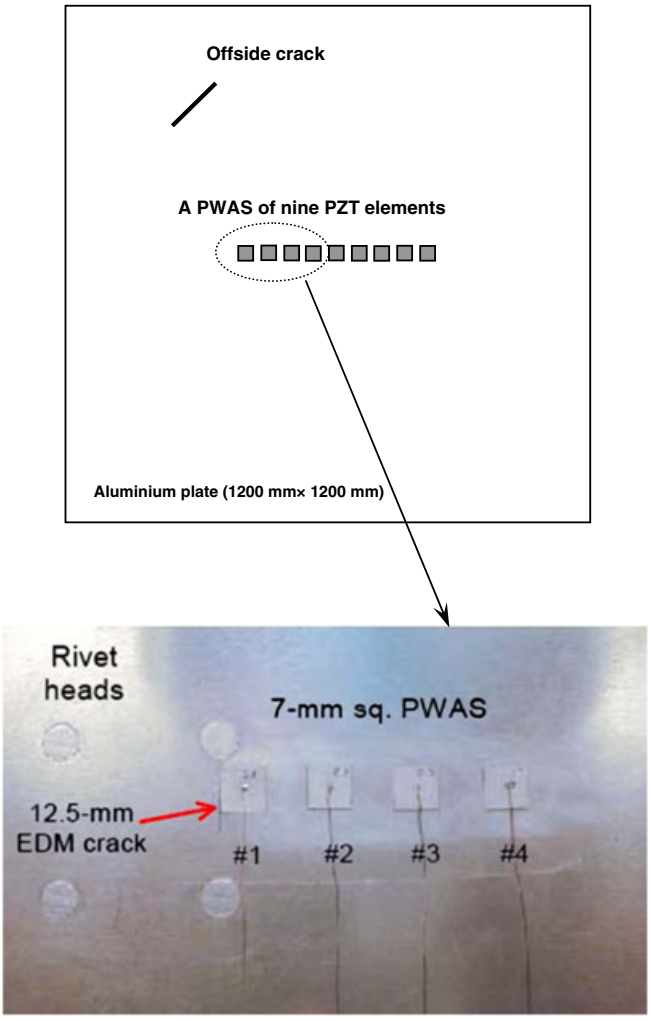

Figure 3. PWAS technique for detecting crack in an aluminium plate (EDM crack: electric discharge machined crack) [23].

DOI: 10.1002/stc

time delays set deliberately. As a result of the time delays, phase differences in the wavefronts activated by individual array elements are created, and the resulting wave is the superposition of wavefronts generated by all elements (i.e. beamforming). By adjusting the time delays properly, the resulting wave can be dominant in a particular direction to present a strong directionality of propagation with significantly improved signal-to-noise ratio (SNR) in comparison with the use of a single actuator–sensor pair. A broad region can thus be scanned by steering the resulting wave in different directions. After being activated to generate waves, array members are shifted immediately to function as sensors for receiving damage-scattered waves by taking advantage of the dual piezoelectric effects.

Most phased-array-based damage identification techniques impose stringent requirement on the relative positions and shape/size of array members because the diagnostic and damage-scattered waves are the superposition of waves generated and received by individual array elements, respectively. An inappropriate allocation of array members can lead to poor recognisability of captured signals. To achieve desired directionality, an array must be designed strategically, and all array members, largely dependent on each other, must be positioned accurately. For example, in a PWAS, a particular wave mode can be activated to dominate the signal energy only when the side length of the square array member equals an odd multiple of one-half the wavelength ($\lambda_{wave}/2$) of such a wave mode [23]. In addition, multi-channel signal generation/acquisition equipment with proper time delay control mechanism is of necessity which may incur high cost.

3. CORRELATIVE SENSOR ARRAY AND CORRELATIVE SENSOR ARRAY-BASED DAMAGE IDENTIFICATION

3.1. Correlative sensor array

An active sensor array approach in line with the outwards accessing scheme aforementioned was developed to facilitate awareness of structural damage and to subsequently locate it. Exploring the time difference between damage-scattered wave signals captured by two individual sensors in the array with the assistance of an integrated processing algorithm based on signal correlation and likelihood searching, the array is named CSA to address these features. Comprising a number of miniaturised PZT wafers collocated closely (therefore featuring a compact dimension), a CSA is displayed schematically in Figure 4. In the CSA, a PZT wafer is centralised, denoted by S_A, serving as an active wave actuator to produce incident diagnostic waves, which is surrounded by another six PZT wafers, functioning as sensors to capture damage-scattered

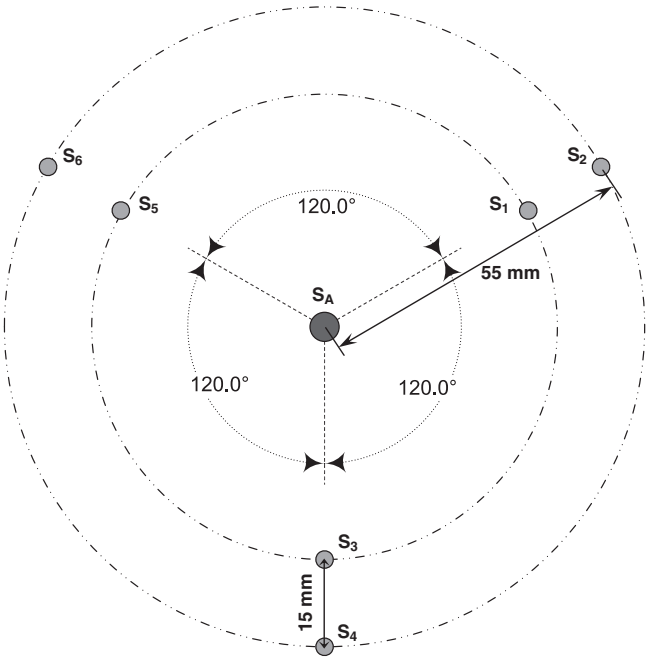

Figure 4. Schematic of a CSA.

DOI: 10.1002/stc

wave signals, denoted by S_i ($i = 1,\ 2,\ \cdots,\ 6$). $S_A - S_i$ stands for the sensing path connecting S_A and S_i. The actuator and two sensors in tandem along a straight line configure a sensing group to offer two sensing paths, and thereby a CSA has three sensing groups: $S_A - S_1/S_A - S_2$, $S_A - S_3/S_A - S_4$ and $S_A - S_5/S_A - S_6$, with an inclination of 120° between any two.

The outer radius of a CSA (55 mm) was determined in order to best reduce the mechanical and electrical coupling between actuators and sensors. Without prior knowledge of possible damage position, circular PZT wafers, with properties detailed in Table I, are selected to generate and capture waves omnidirectionally. In a CSA, S_A is 5 mm in diameter and 0.5 mm in thickness, while six sensors are 3 mm in diameter and 0.25 mm in thickness for each. To enhance SNR of activated signals, the actuator is selected according to an optimal criterion [28]

$$\varphi_{\text{actuator}} = \frac{v_{\text{wave}}}{f} \cdot \left(n + \frac{1}{2}\right) = \lambda_{\text{wave}} \cdot \left(n + \frac{1}{2}\right) \qquad (n = 0,\quad 1,\quad 2,\cdots), \tag{1}$$

where $\varphi_{\text{actuator}}$ is the diameter of the circular PZT actuator; v_{wave}, f and λ_{wave} are the group velocity, frequency and wavelength of the wave mode to be activated, respectively. Considering that the energy consumed to drive a PZT wafer is proportional to $\varphi_{\text{actuator}}$ [29], $n = 0$ in Equation (1) was selected for reducing energy consumption, leading to the present selection of PZT actuator dimension. A thickness of 0.5 mm was selected, allowing working electrical loads up to 200 V to be applied on the actuator without depolarising it. As for the PZT sensors in a CSA, theoretically, a PZT sensor should be as small as possible, and only under such a circumstance is the captured electrical signal proportional to the local strain. Moreover, allowing for the relationship [29]

$$V_{\text{sensor}} \propto \frac{1}{\varphi_{\text{sensor}}}, \tag{2}$$

where φ_{sensor} is the diameter of the circular PZT sensor and V_{sensor} is the output response in the form of electrical voltage, φ_{sensor} should also be kept small for reaching a high magnitude and therefore enhanced SNR. Practically, a PZT wafer when used as a sensor should not be larger than half-wavelength ($\lambda_{\text{wave}}/2$) of the wave mode to be captured. Taking into account the above factors, miniaturised PZT wafers measuring 3 mm in diameter and 0.25 mm in thickness were selected as sensors in a CSA.

3.2. Rationale of correlative sensor array-based damage identification

In recognition of the fact that individual array members in a CSA receive the damage-scattered waves with different ToFs due to the difference in their spatial positions relative to the damage, a damage identification strategy in conjunction with the use of CSA was developed. It basically suggests the position of damage relative to the CSA.

Considering the CSA sketched in Figure 4, the incident diagnostic wave activated by actuator S_A propagates outwards to access the inspection area and will be scattered back by damage (damage is supposed to be at (x_D, y_D) and to be determined) and then will be captured sequentially by two sensors in a sensing group with a certain difference in ToFs. Without loss of generality, focusing on the sensing group comprising S_1 and S_2 and supposing they are located at (x_{S_1}, y_{S_1}) and (x_{S_2}, y_{S_2}), respectively, in a global coordinate system, the difference in ToFs, Δt_{12}, can be defined as

$$\Delta t_{12} = t_{A-D-S_1} - t_{A-D-S_2}, \tag{3}$$

Table I. Material properties of piezoelectric wafer used for developing CSA.

Product name	PI 151
Density (g/cm^3)	7.80
Poisson's ratio	0.31
Charge constant d_{31} (m/V)	-170×10^{-12}
Charge constant d_{33} (m/V)	450×10^{-12}
Relative dielectric constant	1280
Dielectric permittivity p_0 (Farad/meter)	8.85×10^{-12}
Young's modulus E (GPa)	66

DOI: 10.1002/stc

where t_{A-D-S_1} and t_{A-D-S_2} are ToFs of the incident wave propagating from actuator S_A to the damage and then to S_1 and S_2, respectively. Because the time for the incident wave to propagate from S_A to damage is the same for both sensing paths, Equation (3) is simplified as

$$\Delta t_{12} = t_{D-S_1} - t_{D-S_2} \quad , \qquad \text{or} \qquad \Delta t_{12} = \frac{L_{D-S_1}}{V} - \frac{L_{D-S_2}}{V}, \tag{4}$$

where

$$L_{D-S_1} = \sqrt{(x_D - x_{S_1})^2 + (y_D - y_{S_1})^2} \text{ and } L_{D-S_2} = \sqrt{(x_D - x_{S_2})^2 + (y_D - y_{S_2})^2}.$$

V is the group velocity of damage-scattered wave (in this study, it is the damage-scattered lowest-order symmetric Lamb wave mode, to be detailed in Section 5.1); t_{D-S_1} and t_{D-S_2} are ToFs of the damage-scattered waves propagating from the damage to S_1 and S_2, respectively. L_{D-S_1} and L_{D-S_2} are distances from the damage to S_1 and from damage to S_2, respectively.

Mathematically, solutions to Equation (4) configure a locus of roots, and the difference between the distances from any point on the locus to two sensors in a sensing group is a constant, i.e. a hyperbola with S_1 and S_2 being its two foci, shown by the dotted curves in Figure 5. The hyperbola suggests possible locations of damage, which are the perceptions as to the damage existence from the perspective of the sensing group that creates such a hyperbola. A hyperbola has two arms, and the damage is located on the arm closer to the sensor that receives the damage-scattered wave signal earlier than the other.

The hyperbola defined by Equation (4) can be given in a general form in the local coordinate system $(x' - y')$ established for each sensing group (in what follows *prime* in superscript standing for variables in the local coordinate system for each sensing group in a CSA). For the sensing group having S_1 and S_2, as an example, in Figure 6, it is

$$\frac{(x'_D - h')^2}{a^2} - \frac{(y'_D - k')^2}{b^2} = 1, \tag{5a}$$

where

$$h' = \frac{\left(x'_{S_1} + x'_{S_2}\right)}{2} \quad \text{and} \quad k' = \frac{\left(y'_{S_1} + y'_{S_2}\right)}{2}. \tag{5b}$$

The origin is at the central position of actuator S_A (meaning that local coordinate systems for different sensing groups in a CSA share the same origin), and the line connecting S_1 and S_2 is the abscissa axis, with (h', k') being the midpoint of two foci along the local abscissa axis (in a local

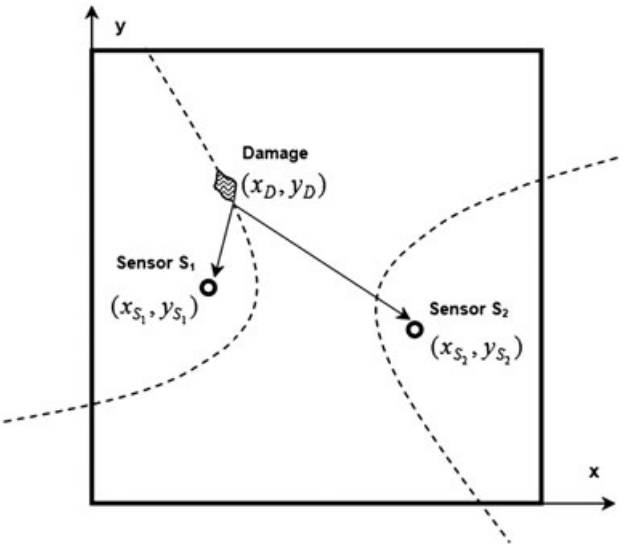

Figure 5. Locus of roots to Equation (4) (dotted curves), forming a hyperbola and indicating possible locations of damage.

DOI: 10.1002/stc

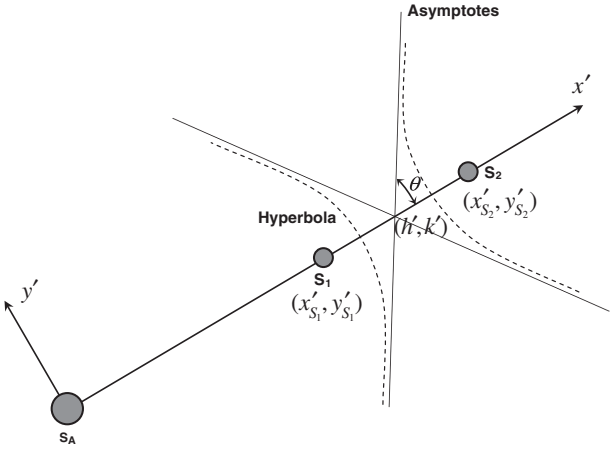

Figure 6. The hyperbola (locus of roots) established by a sensing group in a CSA ($x-y$ standing for the global coordinate system and $x'-y'$ for the local coordinate system for the discussed sensing group).

system, $k' \equiv 0$). a is the semi-major axis of the hyperbola, half the shortest distance between two arms of the hyperbola; b is the semi-minor axis, which can be linked to a by $c = \sqrt{a^2 + b^2}$, where c is the half distance between two foci along the local abscissa axis.

Likewise, upon ascertaining time difference in ToFs from another sensing group in a CSA (say $S_A - S_3/S_A - S_4$ or $S_A - S_5/S_A - S_6$) according to Equation (4), a nonlinear equation group, containing two equations contributed by two sensing groups and involving damage position (x_D, y_D), becomes available. In principle, two hyperbolae defined by the two equations lead to intersection(s), i.e. the solution(s) to the equation group, as shown schematically in Figure 7, which is(are) namely the location(s) of damage (x_D, y_D). The procedure of seeking intersection(s) of a multitude of hyperbolae is actually a process of fusing perceptions as to the damage existence contributed by different sensing groups in a CSA.

Since two sensors of a sensing group in a CSA are apart with a very short distance (15 mm, as indicated in Figure 4), a hyperbola defined by Equation (4) or (5) can be approximated using its asymptotes with acceptable accuracy, which are formulated in the local coordinate system $(x'-y')$ for a sensing group as

$$y' = \pm \frac{b}{a}(x'-h') + k'. \tag{6}$$

Accordingly, the procedure of seeking intersection(s) of hyperbolae established by different sensing groups can be simplified by ascertaining intersection(s) of asymptotes of corresponding hyperbolae. Note that Equation (6) is developed in the local coordinate systems for individual sensing groups in a CSA and an appropriate transformation from individual local systems to a global system is of necessity for analytically obtaining intersection(s) of asymptotes.

Although individual local coordinate systems present different abscissa axes, all of them share the same origin, *viz*, the centre of CSA, making it possible to re-define asymptotes in a global coordinate system $(x-y)$ as

$$y = \pm \tan\left(\arctan\frac{b}{a} + \alpha\right)(x-h) + k = \varepsilon(x-h) + k, \tag{7}$$

where α stands for the inclination between two abscissa axes of the local (x') and global (x) coordinate systems, as indicated in Figure 7; $\varepsilon = \pm \tan\left(\arctan\frac{b}{a} + \alpha\right)$ are the slopes of two asymptotes of a hyperbola. Following the mathematical procedure of seeking solutions to an equation group, the coordinates of intersection(s) of two sets of asymptotes, i.e. (x_D, y_D), in the global coordinate system can be obtained (variables are distinguished by subscripts I and II for two sets of asymptotes),

$$x_D = \frac{\varepsilon_I h_I - \varepsilon_{II} h_{II} - k_I + k_{II}}{\varepsilon_I - \varepsilon_{II}} \quad , \quad \text{and} \quad y_D = \varepsilon_I\left(\frac{\varepsilon_I h_I - \varepsilon_{II} h_{II} - k_I + k_{II}}{\varepsilon_I - \varepsilon_{II}} - h_I\right) + k_I, \tag{8}$$

where ε_I and ε_{II} are slopes of the asymptotes of two sets of hyperbolae, respectively. (h_I, k_I) and (h_{II}, k_{II}) are defined by Equation (5b). In principle, two sets of hyperbolae, contributed by two sensing

DOI: 10.1002/stc

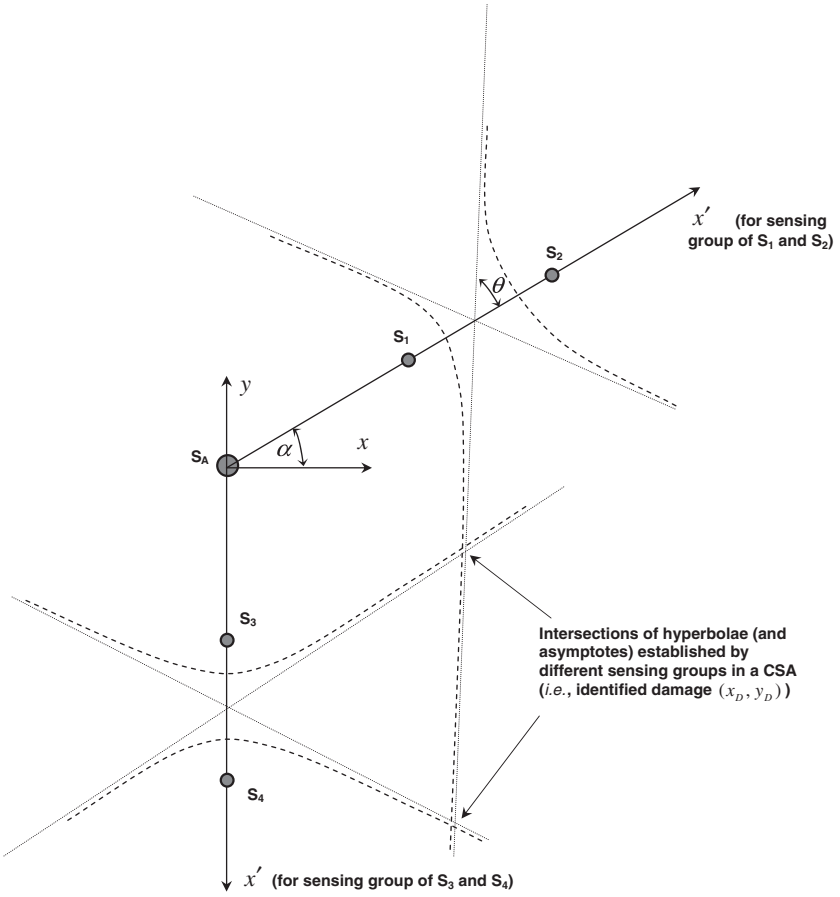

Figure 7. CSA-based damage triangulation strategy using two sensing groups ($x-y$ standing for the global coordinate system and $x'-y'$ for the local coordinate systems for different sensing groups in the CSA).

groups in a CSA, present four asymptotes (two for each), potentially leading to a multitude of intersections, at one of which the damage locates whereas the rest are pseudo solutions that can be excluded by introducing another sensing group in the CSA and seeking the common intersection(s) of all three sets of asymptotes.

The underlying mechanism of CSA-based damage identification implies that different sensing groups in a CSA work independently when developing perceptions as to damage (Equation (4)), and it thereby tolerates a certain degree of imprecision in installing individual sensors in a CSA or malfunction of partial sensing groups, without compromising identification accuracy. It shows advantages over conventional outwards accessing schemes which often impose demanding requirements on the relative positions and shape/size of individual array members.

4. INTEGRATED SIGNAL PROCESSING ALGORITHM

4.1. Ascertainment of time difference using signal correlation

In the CSA-based damage identification strategy, precise ascertainment of time difference in ToFs between the damage-scattered waves captured by two sensors of a sensing group is a prerequisite to deliver accurate identification. However as a consequence of very short distance between two sensors in a sensing group, the two captured signals were observed to be identical in waveform although with a slight discrepancy in arrival time, as one example shown in Figure 8. Such discrepancy is often at an inconspicuous level, posing difficulty in precisely extracting time difference in ToFs. An ascertainment approach in terms of signal correlation processing was therefore developed.

DOI: 10.1002/stc

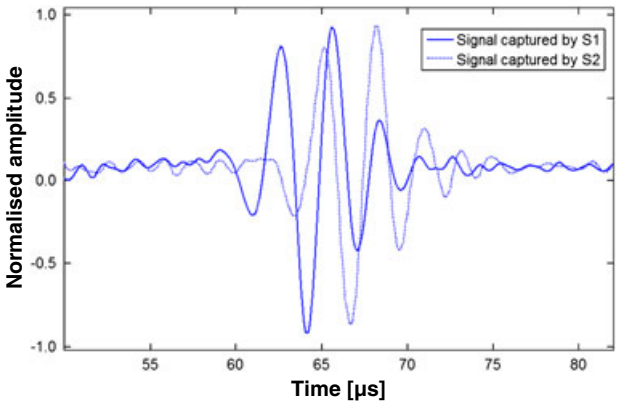

Figure 8. Representative Lamb wave signals captured by a sensing group in CSA.

Considering that two signals captured by two sensors are x_i and y_i (both have the same length ($i = 1, 2, \cdots, N$, discretised with N sampling points)), the correlation coefficient, λ_{xy}, of these two signals is defined as [7]

$$\lambda_{xy} = \frac{N\sum_{i=1}^{N} x_i y_i - \sum_{i=1}^{N} x_i \sum_{i=1}^{N} y_i}{\sqrt{N\sum_{i=1}^{N} x_i^2 - \left(\sum_{i=1}^{N} x_i\right)^2} \cdot \sqrt{N\sum_{i=1}^{N} y_i^2 - \left(\sum_{i=1}^{N} y_i\right)^2}}, \tag{9a}$$

or

$$\lambda_{xy} = \frac{C_{xy}}{\sigma_x \cdot \sigma_y} = \frac{\sum_{i=1}^{N} (x_i - \mu_x)\left(y_i - \mu_y\right)}{\sqrt{\sum_{i=1}^{N} (x_i - \mu_x)^2} \cdot \sqrt{\sum_{i=1}^{N} \left(y_i - \mu_y\right)^2}}, \tag{9b}$$

where C_{xy}, μ and σ are the covariance, mean and standard deviation of x_i and y_i, distinguished by subscripts for two signals. When x_i is very similar to y_i, the correlation coefficient defined by Equation (9a) or (9b) approaches unity; the greater the similarity between two signals, the closer to unity is the coefficient.

λ_{xy} was therefore used as an indicator to calibrate the degree of similarity between signals captured by two sensors of a sensing group in a CSA. In brief, one of the two signals was shifted along the time axis relative to the other with a tiny increment, and their correlation coefficients were calculated using Equation (9a) or (9b) upon each shift. When the correlation coefficient between two signals reached the extremum upon a particular shift, it was deemed that the time used for shifting the signal was namely the time difference in ToFs between the damage-scattered waves captured by these two sensors.

4.2. Moving-window-based likelihood searching

The above processing based on signal correlation establishes the framework for determining the time difference in ToFs. To improve the efficiency and accuracy of such a process, an MWLS algorithm was further developed. Suppose that the damage-scattered wave component in a signal is w in length, the same as the length of the diagnostic wave signal if wave dispersion and distortion with propagation distance are ignored. The damage-scattered wave component is always first observed in a signal earlier than boundary reflections because the outwards accessing scheme is adopted in CSA. In the MWLS algorithm, a rectangular window of u in length (u is slightly greater than w, to be discussed in a subsequent section) is shifted along one of the two signals captured by two sensors of a sensing group, discretely with increment δ, throughout the time period of interest (sufficiently long so as to include all concerned wave modes). Such a shifting procedure is called *primary shift* in this study. By way of illustration, Figure 9 shows four consecutive primary shifts.

DOI: 10.1002/stc

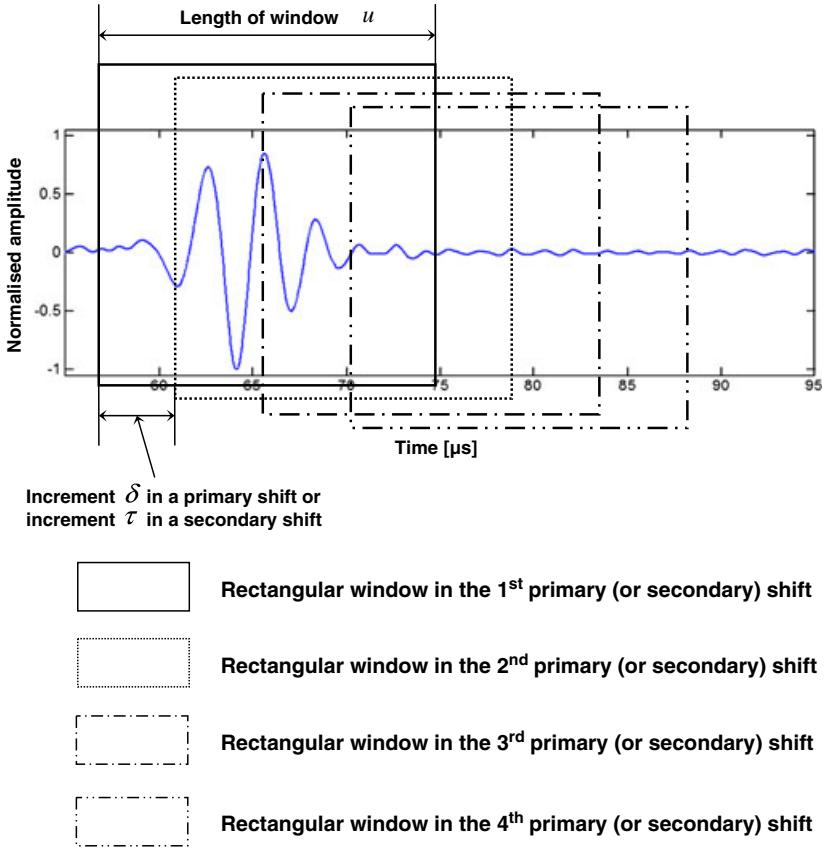

Figure 9. Schematic illustration of four consecutive primary (or secondary) shifts in MWLS (the indicated increment being δ for a primary shift or being τ for a secondary shift).

Synchronously, the same rectangular window and primary shift are applied on the other signal, whereas upon each primary shift, the rectangular window is further moved forwards along the time axis with increment τ (τ is much smaller than δ). Such a shifting procedure is called *secondary shift*, which can also be elucidated using Figure 9. Throughout the study, τ was set as the interval of two neighbouring sampling moments, the minimum that can be achieved, which was one-twenty-fifth of δ.

Under each primary shift, correlation coefficients of the windowed fragments in two signals are calculated upon completion of every single secondary shift. In the case that neither of the two windowed fragments contains any damage-scattered waves or boundary reflections, they present a poor similarity and therefore a low correlation coefficient because random measurement noise is dominant in the windowed fragments; in contrast, if both windowed signal fragments contain damage-scattered waves or boundary reflections which dominate the signal energy, the correlation coefficient is expected to be great. For illustration, correlation coefficients calculated upon completion of every single secondary shift under a particular primary shift, for the two signals shown in Figure 8, is displayed in Figure 10 to observe that, at the 126th secondary shift under this particular primary shift, two windowed fragments claim the highest similarity.

The same manipulation is then applied to every single primary shift throughout the time period of interest. For the example signals in Figure 8, Figure 11(a) three-dimensionally shows the distribution of calculated correlation coefficients of two signals under five consecutive primary shifts and subsequent secondary shifts. To benefit ascertainment of the greatest correlation coefficient during the shifting, the diagram is locally zoomed in and presented three-dimensionally and two-dimensionally in Figure 11(b) and (c), respectively. The grey scale in Figure 11(c) indicates the value of calculated correlation coefficients, and the lighter the grey scale the greater the correlation coefficient is. It can be seen that, upon completion of the 126th secondary shift under the third primary shift, the coefficient reaches its extremum. Conclusion can thereby be drawn that the time used for this secondary shift

DOI: 10.1002/stc

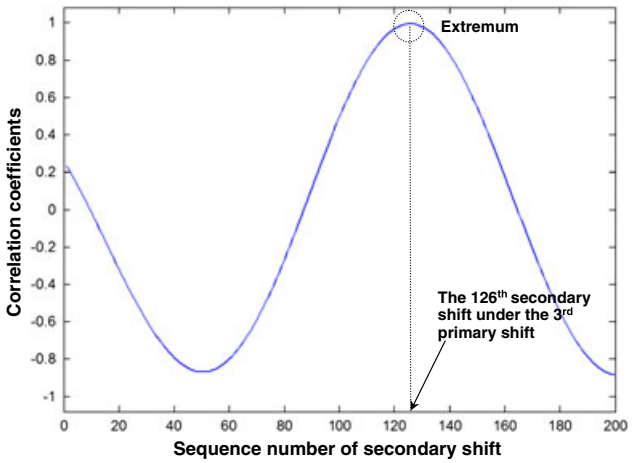

Figure 10. Calculated correlation coefficients of windowed fragments of two signals in Figure 8 versus sequence number of the secondary shift under a primary shift.

under its corresponding primary shift, *viz*, 126 sampling intervals, is namely the difference in ToFs between the damage-scattered waves captured by two sensors.

In some particular cases that the windowed fragments contain partial rather than full damage-scattered wave components, their correlation can be weak under the influence of broadband measurement noise, leading to erroneous ascertainment. To insure inclusion of full damage information for MWLS, the length of the rectangular window, u, in this study was selected greater than that of the damage-scattered wave w as

$$u = w + 2\delta. \tag{10}$$

By such a means, at least one windowed fragment during the primary shift throughout the time period of interest includes the full length of the damage-scattered wave component, guaranteeing the accuracy of searching. On the other hand, in a secondary shift with increment τ, only when the damage is located right on the line connecting two sensors in a sensing group will the time difference in ToFs be maximum, and it will be the time used for the damage-scattered wave to travel between two sensors. Allowing for this, the secondary shifting is limited to such a range that the shift would not exceed the above-addressed maximum time difference.

5. APPLICATION: IDENTIFICATION OF DAMAGE IN PLATE-LIKE STRUCTURES

5.1. Finite element simulation

The feasibility of using CSA and its integrated signal processing algorithm for locating damage in plate-like structures was demonstrated via finite element (FE) simulation. A CSA was supposed to be surface-installed at the approximate centre of an aluminium plate. The aluminium plate was 600 mm × 600 mm × 1.5 mm in size and supported with all its four edges. The plate was three-dimensionally modelled using eight-node brick solid elements. To insure simulation precision, the largest dimension of FE elements was less than 1 mm, and the plate was divided into multi-layer in thickness, guaranteeing that at least 10 elements were allocated per wavelength of the incident diagnostic wave, which has been demonstrated sufficient to portray the characteristics of elastic waves in a thin plate [30]. A through-thickness hole of 16 mm in diameter was assumed in the plate, 115 and 282 mm away from the left and upper edges of the plate, respectively, as seen in Figure 12(a). The location of damage was selected randomly. The FE mesh near the through-thickness hole was particularly densified. The FE model of this aluminium plate is exhibited in Figure 12(b).

In a thin plate, both the symmetric and anti-symmetric Lamb wave modes co-exist, and in particular S_0 and A_0 are the lowest-order symmetric and anti-symmetric modes, respectively. In this study, the S_0 mode was selected for damage identification because of, in contrast to A_0, (1) its lower attenuation (the

DOI: 10.1002/stc

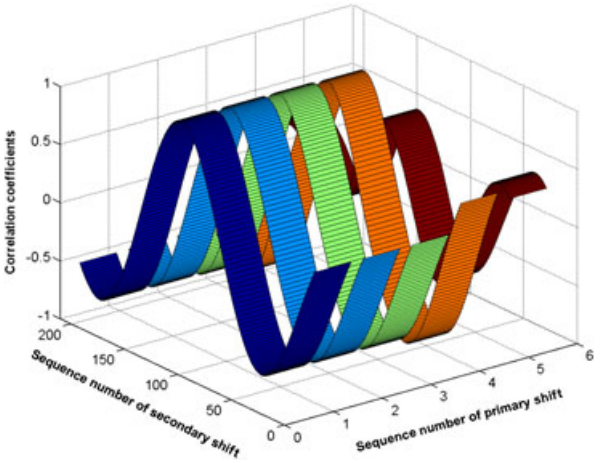

(a)

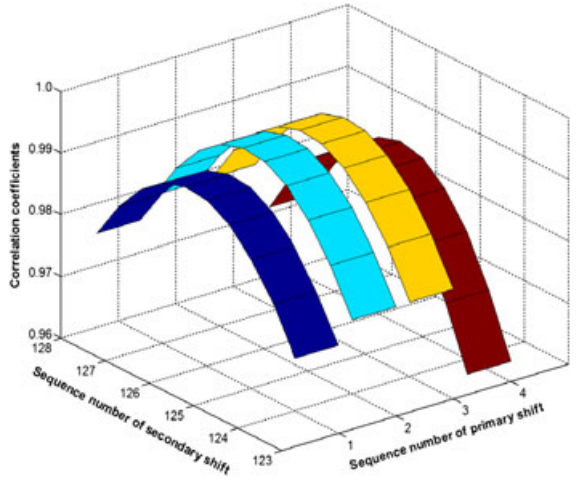

(b)

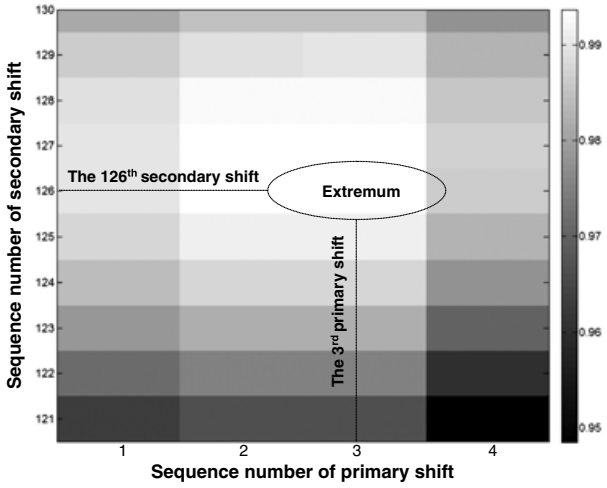

(c)

Figure 11. (a) Calculated correlation coefficients of windowed fragments of two signals in Figure 8 under five consecutive primary shifts and subsequent secondary shifts; (b) zoomed-in part of (a) in three-dimensional presentation; and (c) zoomed-in part of (a) in two-dimensional presentation.

DOI: 10.1002/stc

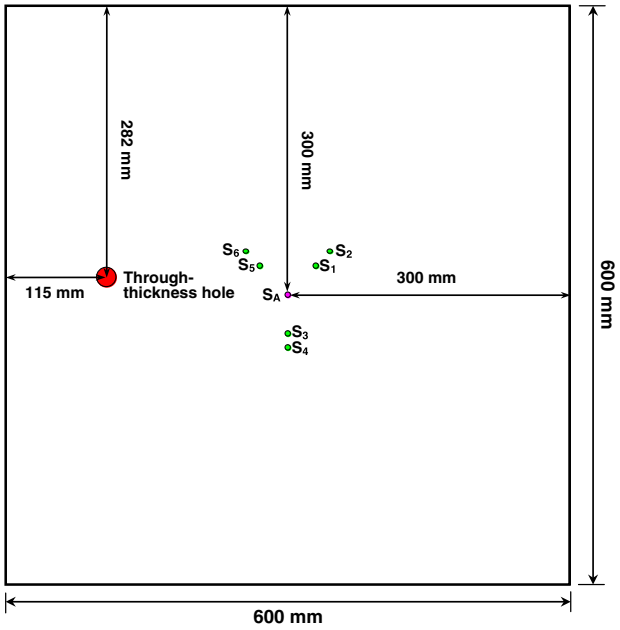

(a)

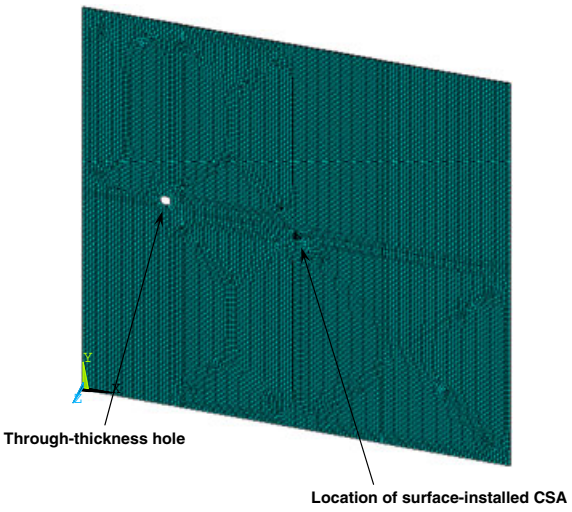

(b)

Figure 12. (a) An aluminium plate containing a through-thickness hole and a surface-mounted CSA; and (b) FE model of the plate in (a).

A_0 mode has the dominant out-of-plane movement of particles, leaking partial energy to the surrounding medium, whereas the S_0 mode has mostly in-plane displacement and its energy is confined within the plate. Therefore, S_0 manifests lower attenuation during propagation than A_0); (2) faster propagation velocity, implying that complex wave reflection from structural boundary may be avoided; and (3) lower dispersion, facilitating signal interpretation. In addition, the S_0 mode presents stronger reflection from through-thickness damage than the A_0 mode [12], suitable for the CSA-based damage identification because a CSA substantially relies on the damage-reflected waves.

To activate the S_0 mode in FE simulation, a pre-developed piezoelectric actuator model [30] was employed to simulate the actuator, S_A. Uniform radial displacement constraints (within $x-y$ plane) were applied on FE nodes of the upper surface of the actuator, as shown in Figure 13, to dominantly generate the S_0 mode. With this actuator model, three-cycle *Hanning* window-modulated sinusoid tonebursts at a central frequency of 300 kHz were activated as the incident diagnostic wave. This selected frequency is

DOI: 10.1002/stc

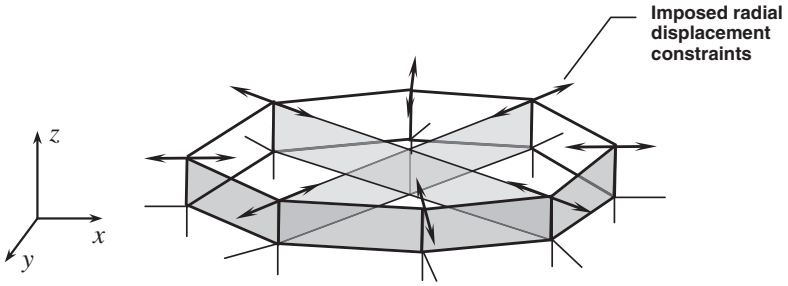

Figure 13. A pre-developed FE model for simulating piezoelectric actuator (uniform radial displacement constraints applied on FE nodes of the upper surface of the actuator to dominantly generate S_0).

lower than the cut-off frequencies of higher-order modes in the discussed aluminium plate, and as a consequence only the S_0 and A_0 mode co-exist. At this excitation frequency, the group velocity of S_0 in the discussed thin plate (1.5 mm in thickness) is around 5100 m/s. Sensor S_i ($i = 1, 2, \cdots, 6$) was modelled with a pre-developed sensor model [30]. Dynamic FE simulation was accomplished using commercial FE code ANSYS®. The step of calculation time was less than the ratio of the minimum distance of any two adjoining FE nodes to the velocity of S_0. As some representative results obtained from FE simulation, Figure 14 exemplarily displays the signals captured by the sensing group comprising sensors S_5 and S_6 in the surface-mounted CSA.

5.2. Experimental validation

The above simulation was experimentally testified. The surface-installed CSA was instrumented with a signal generation and acquisition system shown schematically in Figure 15 [30]. The incident diagnostic wave, the same as that used in the above simulation, was generated with an arbitrary waveform generator (HIOKI® [manufactured by HIOKI Corporation, Nagano, Japan] 7075), amplified to 35 $V_{p\text{-}p}$ with a linear signal amplifier (Piezo Systems® [manufactured by PIEZO SYSTEMS, INC., Woburn, MA., 01801, USA] EPA-104) and then applied on S_A in the CSA. The signals were in turn captured by S_i ($i = 1, 2, \cdots, 6$) using a digital oscilloscope (Agilent® [manufactured by Agilent Technologies Ltd., Santa Clara, CA., USA] INFINIIUM 54810A) at a sampling rate of 50 MHz. All the captured signals were pre-processed including averaging, offsetting and de-nosing. Upon screening broadband noise using wavelet transform [30], the wave components in the active excitation frequency range (around 300 kHz) were canvassed. To compare with simulation, the pre-processed wave signals captured by the same sensing group are displayed in Figure 16, matching well with those obtained in simulation shown in Figure 14.

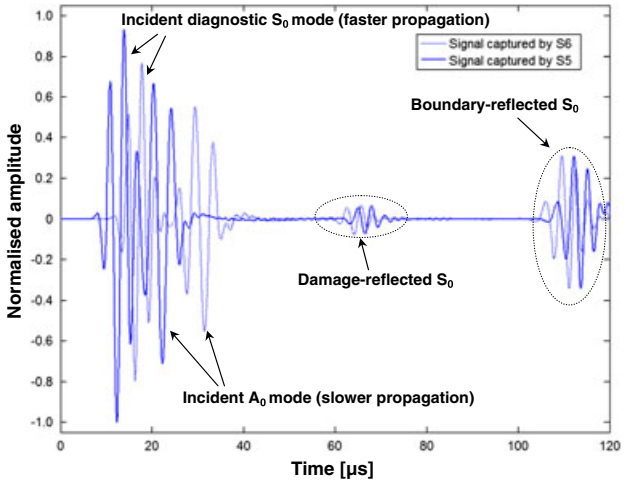

Figure 14. Lamb wave signals numerically captured via a representative sensing group comprising S_5 and S_6 in the CSA installed on an aluminium plate containing a through-thickness hole.

DOI: 10.1002/stc

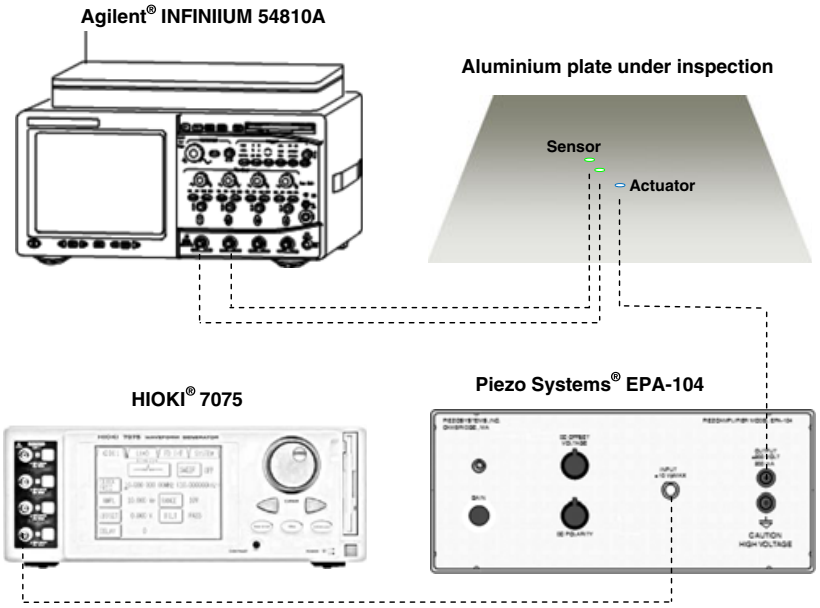

Figure 15. Set-up for experimental validation.

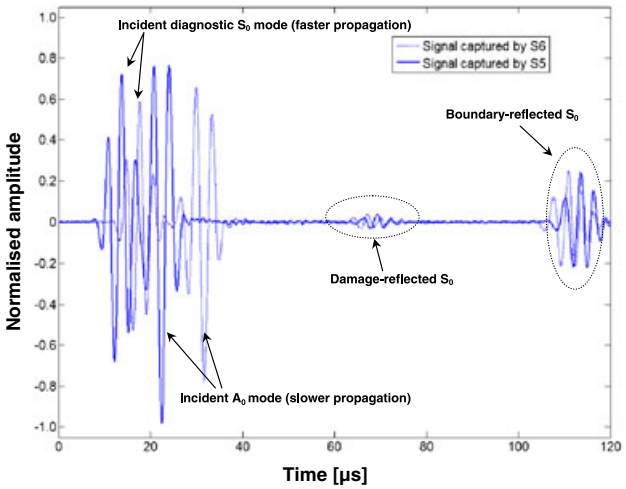

Figure 16. Lamb wave signals experimentally captured via a reprehensive sensing group comprising S_5 and S_6 in the CSA installed on an aluminium plate containing a through-thickness hole.

5.3. Identification results

With the diagnostic signal being three-cycle tonebursts at 300 kHz, the length of the damage-scattered wave component w is approximately $3/(300 \times 10^3\ \text{Hz}) = 10\ \mu\text{s}$ if dispersion and distortion of wave with propagation distance are ignored. A rectangular window of 20 μs in length was accordingly selected in terms of Equation (10) ($u = w + 2 \cdot \delta = 20\ \mu\text{s}$), if the increment of primary shift δ was set as 5 μs. After being pre-processed and applied with the integrated algorithm including signal correlation and MWLS, time differences in ToFs between the damage-scattered Lamb waves captured by two sensors of three sensing groups in the CSA were ascertained, summarised in Table II. The velocities of different wave modes obtained via simulation and experimental measurement are listed in Table III. With acquired time differences, the through-thickness hole in the plate was located in terms of Equation (8), graphically shown in Figure 17 and detailed in Table IV. Satisfactory identification precision was achieved.

DOI: 10.1002/stc

Table II. Measurement and identification results obtained through FE simulation and experimental validation: time differences in ToFs between damage-scattered Lamb waves captured by two sensors of three sensing groups in the CSA [μs]*.

	S_1 and S_2	S_3 and S_4	S_5 and S_6
FE simulation	−3.20	−1.00	2.52
Experiment	−3.22	−1.10	2.56

*Negative sign standing for those cases that the sensor of a sensing group on the inner periphery receives damage-reflected waves earlier than the sensor on the outer periphery.

Table III. Measurement and identification results obtained through FE simulation and experimental validation: propagation velocities of different Lamb wave modes [m/s].

	S_0 mode	A_0 mode
FE simulation	5087.6	2846.6
Experiment	5045.9	3042.9

Note that, more strictly speaking, the incident diagnostic waves first interact with the edge of the damage, and it is thereby envisaged that the identified damage location by using CSA is the edge of the damage with the shortest distance to the CSA rather than the damage centre. But allowing for the small size of damaged zone contrasting with the entire inspection region, such an error is negligible. In order to quantify such an error, another two damage scenarios were further taken into account in the simulation, in which the through-thickness hole featured different diameters (20 and 24 mm, respectively). The identification results are listed in Tables V. Both Tables IV and V indicate that damage size in a reasonable range (see Table IV and V for percentage of the damaged zone with regard to the entire inspection area) would not phenomenally impair the detection accuracy of this approach.

6. DISCUSSION

6.1. Effective detection area

A prominent advantage of the outwards accessing scheme over the inwards accessing scheme is that the incident diagnostic waves often encounter damage, if any, earlier than structural boundaries, and as a consequence the damage-scattered waves are observed first in a captured signal without interferences of complex boundary reflections, benefiting signal processing and interpretation. However, propagating at a faster velocity, the damage-reflected S_0 mode may catch up with the outgoing A_0 mode activated by the actuator that propagates at a lower velocity. The overlapping between the S_0 and the A_0 modes complicates the signal appearance. To insure that the damage-reflected S_0 mode would not overlap the outgoing A_0 mode, the following simple criteria should be met

$$\frac{L_{A-D} + L_{D-S_i}}{V_{S_0}} \geq \frac{L_{A-S_i}}{V_{A_0}} + w, \tag{11}$$

where L_{A-D}, L_{D-S_i} and L_{A-S_i} are the distances between the damage and actuator, between the damage and sensor S_i and between the actuator and S_i, respectively. w is the length of the damage-scattered wave component in a signal, the same as that of the incident diagnostic wave signal if wave dispersion and distortion are ignored. V_{S_0} and V_{A_0} are the propagation velocities of the S_0 and A_0 modes, respectively, referring to Table III. Provided that equality condition is tenable in Equation (11) (i.e. the damage is located right at the ellipses shown in Figure 18), the damage-reflected S_0 mode follows the outgoing A_0 mode immediately in a captured signal, but both are still recognisable. Based on Equation (11), a conclusion can be drawn that the CSA-based damage identification strategy can offer an effective detection area throughout the plate except those regions in grey as shown in Figure 18 (called 'blind zone'). The blind zone is shaped by three ellipses which were obtained by considering S_2, S_4 and S_6 in Equation (11), respectively (compared with those captured by sensors located at the inner periphery of a CSA (S_1, S_3 and S_5); the damage-reflected S_0 mode received by S_2, S_4 and S_6 at the outer

DOI: 10.1002/stc

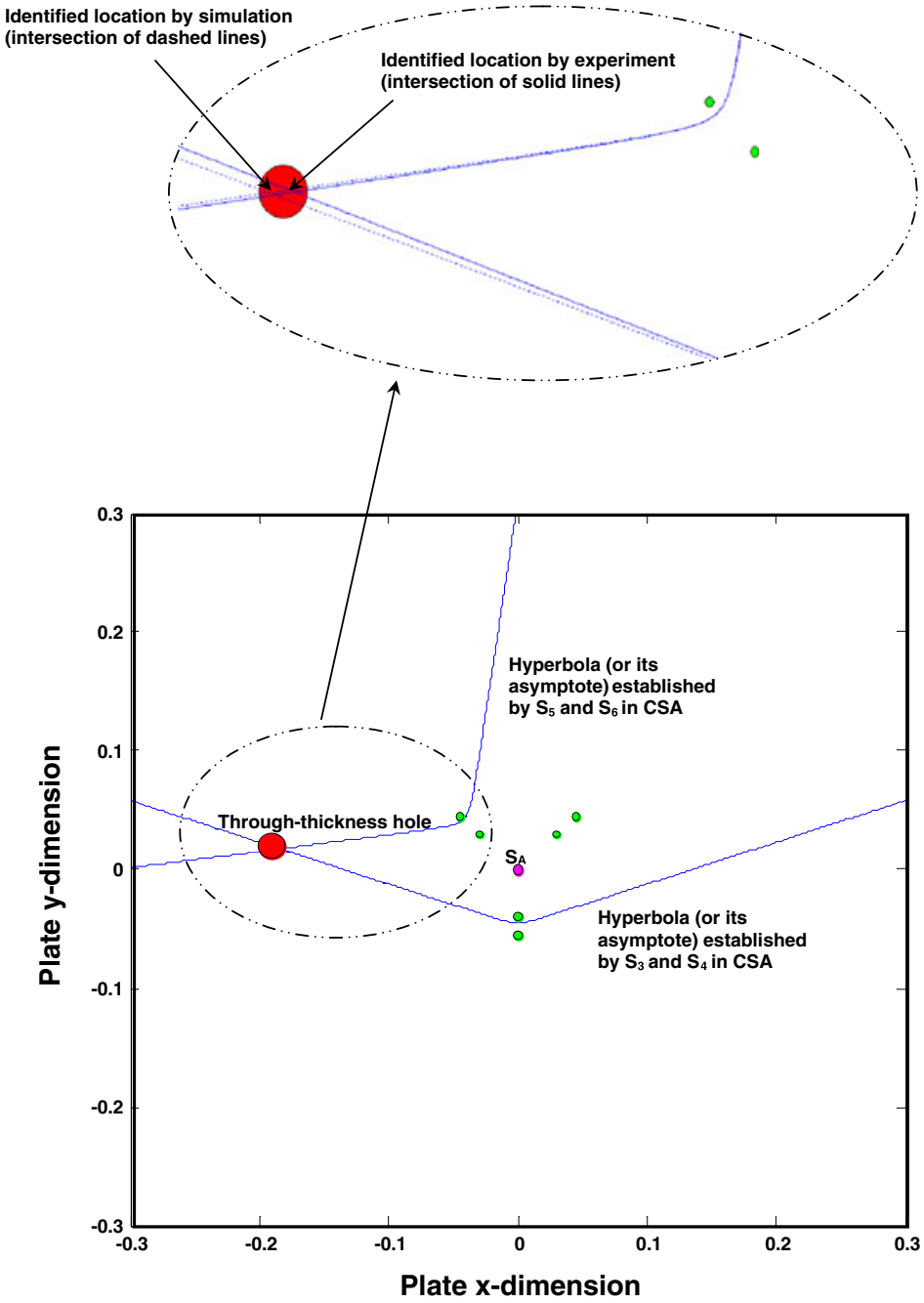

Figure 17. Identification results for the through-thickness hole using CSA-based identification strategy (grey circle: actual damage; dotted line in zoomed-in part: asymptote of the hyperbola obtained by simulation; solid line in zoomed-in part: asymptote of the hyperbola obtained by experiment; unit: m).

Table IV. Measurement and identification results obtained through FE simulation and experimental validation: identification results of a through-thickness hole (Ø16 mm, 0.056% of inspection region) in the aluminium plate[@].

Actual location [mm]	From FE simulation [mm]	Maximum simulation error [%]	From experiment [mm]	Maximum experiment error [%]
(−185, 18)	(−189, 19)	5.56	(−182, 19)	5.56

[@]In the global coordinate system where the origin is at the central position of the CSA and the abscissa axis is in parallel with the lower edge of the aluminium plate.

DOI: 10.1002/stc

Table V. Measurement and identification results obtained through FE simulation and experimental validation: identification results of through-thickness holes of different sizes in the aluminium plate[@].

Damage diameter [mm]	Actual location [mm]	FE simulation [mm]	Maximum error [%]
20 (0.087% of inspection region)	(−185, 18)	(−183, 18)	1.08
24 (0.126% of inspection region)	(−185, 18)	(−182,18)	1.62

[@]In the global coordinate system where the origin is at the central position of the CSA and the abscissa axis is in parallel with the lower edge of the aluminium plate.

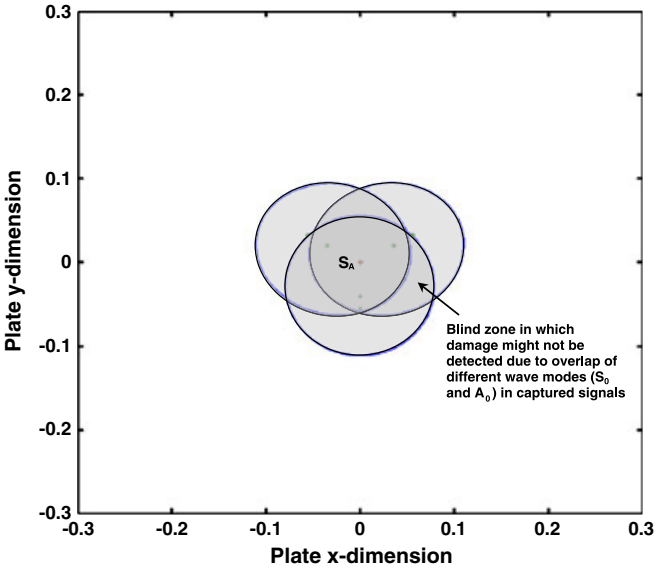

Figure 18. Effective detection area for CSA-based damage identification strategy.

periphery are more likely to overlap the outgoing A_0 mode. Therefore, sensors S_2, S_4 and S_6 were used to determine the blind zones).

6.2. Sensitivity

In CSA-based damage identification, hyperbolae established by individual sensing groups in a CSA were approximated using their corresponding asymptotes defined by Equation (6). The slope of the asymptote ε (a hyperbola possesses two asymptotes, and for convenience of discussion and without loss of generality we focus on the asymptote that has a positive slope in the local coordinate system) is

$$\varepsilon = \frac{b}{a} = \sqrt{\frac{c^2-a^2}{a}} = \sqrt{\frac{c^2}{a^2}-1} \qquad \text{(in the local coordinate system)}, \tag{12a}$$

and it has

$$a = c \cdot \sqrt{\frac{1}{\varepsilon^2+1}} = c \cdot \sqrt{\frac{1}{(\tan(\theta))^2+1}}, \tag{12b}$$

where θ is the inclination between the discussed asymptote and the local abscissa axis, as indicated in Figures 6 and 7. It also has, in terms of the definition of a hyperbola,

$$2a = \Delta t \cdot V, \tag{13}$$

where Δt is the time difference between the damage-scattered waves captured by two sensors in a sensing group, and V is the group velocity of the damage-scattered wave mode. Substituting Equation (12b) in Equation (13) yields

$$\Delta t = \frac{2c}{V} \cdot \sqrt{\frac{1}{(\tan(\theta))^2+1}}. \tag{14}$$

DOI: 10.1002/stc

The derivative function of Equation (14) with regard to θ is graphically described in Figure 19. It can be seen that at a particular θ, the relative changes in Δt as a result of change in the damage location, *viz*, $\frac{\partial(\Delta t)}{\partial\theta}$, is different considerably. This implies that, when damage locates in some regions associated with θ, the CSA might be insensitive to changes in the damage location, and these regions are called 'dull regions' in this study. For the above discussed application, the signal acquisition hardware offered a sampling rate of 50 MHz, and the minimum recognisable change in Δt was thereby $1/50\,\text{MHz} = 2\times10^{-8}$ s, corresponding to the case that $\theta = 16^0$ in terms of Equation (14), as seen in Figure 19. It alludes to the fact that a dull region associated with $\theta \le 16^0$ exists for each sensing group in the CSA, as shadowed in Figure 20. Changes in the location of damage in the dull region may not induce recognisable changes in

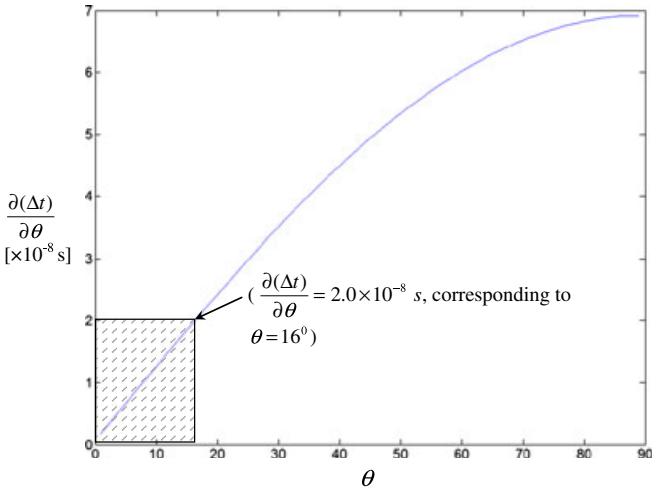

Figure 19. Derivative function of Equation (14) with regard to θ.

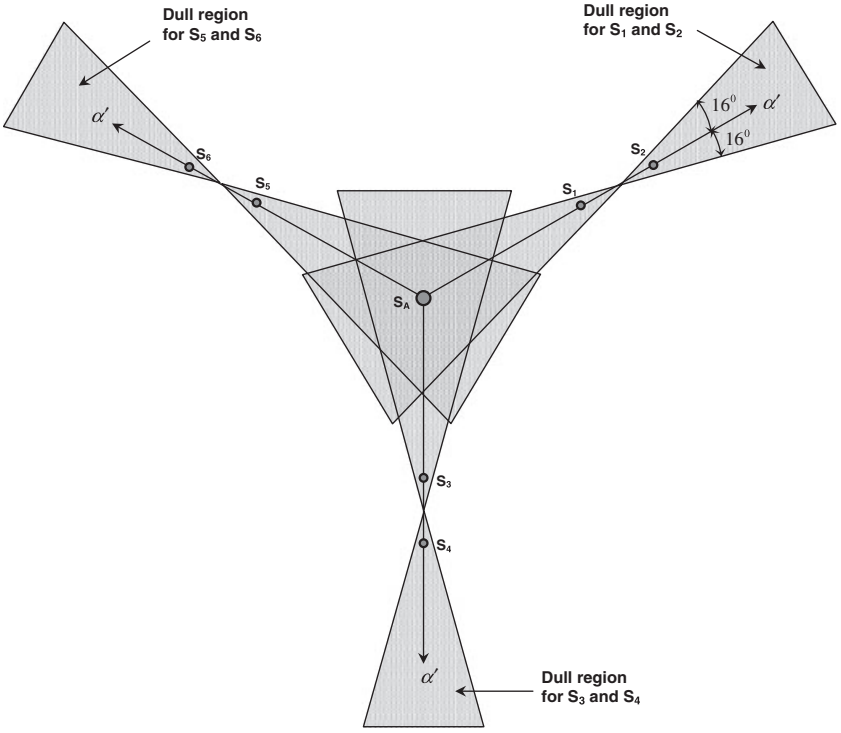

Figure 20. Schematic of dull regions for CSA-based damage identification strategy.

DOI: 10.1002/stc

difference in ToFs, posing difficulty in accurately locating damage. However, a CSA exploits three sensing groups at the same time for locating damage, and under such a circumstance only when the damage is located right in the collective area of three dull regions may the damage not be exactly pinpointed.

It is noteworthy that some types of damage present orientation-specific geometric features (for instance, a crack with a dominant length in a particular dimension or polygonal damage with individual edges); under such a circumstance, the damage exerts strong influence on the directivity of wave propagation, and the damage-scattered waves may not be efficiently captured by some sensing groups in the CSA. This might reduce the identification accuracy. Such an issue was elaborated in authors' work reported elsewhere [31]. In addition, it is understandable that the proposed damage identification strategy based on the use of CSA can also be applicable to detection of multi-damage if two or more sets of CSA, positioned at different locations, are used simultaneously.

7. CONCLUSIONS

With the aid of an integrated signal processing algorithm including signal correlation and MWLS, an active sensor array comprising a number of miniaturised piezoelectric wafers aligned strategically was developed for guided-wave-based damage identification, named CSA. Exploring time difference of Lamb wave signals captured by individual array members, a CSA is able to detect and locate structural damage. Satisfactory accuracy in identifying a through-thickness hole in an aluminium plate, as an application, was achieved through FE simulation and experimental validation, demonstrating effectiveness of CSA-based damage identification for plate-like structures. Such an active sensor array approach presents some advantages over conventional array techniques including tolerance to inaccurate installation of individual sensors in the array. As observed, a CSA with the current configuration shows certain limitations in effectively detecting damage in some areas within the inspection region, forming blind and dull zones, which however can be circumvented to a certain degree by introducing more sets of CSA.

ACKNOWLEDGEMENTS

Authors are grateful to the Research Grants Council of Hong Kong for General Research Fund (GRF) 527008. The work also partially benefitted from Grant A-PE1F provided by the Hong Kong Polytechnic University.

REFERENCES

1. Michaels JE, Croxford AJ, Wilcox PD. Imaging algorithms for locating damage via *in situ* ultrasonic sensors. In *Proceedings of SAS 2008—IEEE Sensors Applications Symposium*, Atlanta, GA. USA, 12–14, February. IEEE: Piscataway, NJ 2008; 63–67.
2. Kundu T, Das S, Jata KV. Health monitoring of a thermal protection system using Lamb waves. *Structural Health Monitoring: An International Journal* 2009; **8**(1):29–45.
3. Lin X, Yuan FG. Diagnostic Lamb waves in an integrated piezoelectric sensor/actuator plate: analytical and experimental studies. *Smart Materials and Structures* 2001; **10**:907–913.
4. Kim SB, Sohn H. Instantaneous reference-free crack detection based on polarization characteristics of piezoelectric materials. *Smart Materials and Structures* 2007; **16**:2375–2387.
5. Tobias A. Acoustic-emission source location in two dimensions by an array of three sensors. *Non-Destructive Testing* 1976; **9**(1):9–12.
6. Fromme P, Wilcox PD, Lowe MJS, Cawley P. On the development and testing of a guided ultrasonic wave array for structural integrity monitoring. *IEEE Transactions on Ultrasonics, Ferroelectrics, and Frequency Control* 2007; **33**:777–785.
7. Zhao X, Gao H, Zhang G, Ayhan B, Yan F, Kwan C, Rose JL. Active health monitoring of an aircraft wing with embedded piezoelectric sensor/actuator network: I. defect detection, localization and growth monitoring. *Smart Materials and Structures* 2007; **16**:1208–1217.
8. Staszewski WJ, Pierce SG, Worden K, Philp WR, Tomlinson GR, Culshaw B. Wavelet signal processing for enhanced Lamb wave defect detection in composite plates using optical fiber detection. *Optical Engineering* 1997; **36**:1877–1888.
9. Badcock RA, Birt EA. The use of 0–3 piezocomposite embedded Lamb wave sensors for detection of damage in advanced fibre composites. *Smart Materials and Structures* 2000; **9**:291–297.
10. Boller C. Ways and options for aircraft structural health management. *Smart Materials and Structures* 2001; **10**:432–440.
11. Ihn J-B, Chang F-K. Pitch-catch active sensing methods in structural health monitoring for aircraft structures. *Structural Health Monitoring: An International Journal* 2008; **7**(1):5–19.
12. Su Z, Ye L, Lu Y. Guided Lamb waves for identification of damage in composite structures: a review. *Journal of Sound and Vibration* 2006; **295**:753–780.
13. Qing XP, Beard SJ, Kumar A, Ooi TK, Chang F-K. Built-in sensor network for structural health monitoring of composite structure. *Journal of Intelligent Material Systems and Structures* 2007; **18**:39–49.

DOI: 10.1002/stc

14. Wang Q, Yuan SF. Baseline-free imaging method based on new PZT sensor arrangements. *Journal of Intelligent Material Systems and Structures* 2009; **20**: 1663–1673.
15. Diamanti K, Soutis C, Hodgkinson JM. Piezoelectric transducer arrangement for the inspection of large composite structures. *Composites: Part A* 2007; **38**:1121–1130.
16. Kudela P, Ostachowicz W, Zak A. Damage detection in composite plates with embedded PZT transducers. *Mechanical Systems and Signal Processing* 2008; **22**:1327–1335.
17. Staszewski WJ, Worden K. Overview of optimal sensor location methods for damage detection. In *Proceedings of the 8th SPIE Symposium on Smart Structures and Materials*. (*Conference on Modeling, Signal Processing and Control of Smart Structures*), Rao, VS (ed.). Newport Beach, CA, USA, vol. **4326**, SPIE: Bellingham WA 98227–0010 USA 2001; 179–187.
18. Lee BC, Staszewski WJ. Sensor location studies for damage detection with Lamb waves. *Smart Materials and Structures* 2007; **16**:399–408.
19. Flynn EB, Todd MD. Optimal placement of piezoelectric actuators and sensors for detecting damage in plate structures. *Journal of Intelligent Material Systems and Structures* 2010; **21**(2):265–274.
20. Lin M, Chang F-K. The manufacture of composite structures with a built-in network of piezoceramics. *Composites Science and Technology* 2002; **62**:919–939.
21. Hurlebaus S, Gaul L. Smart layer for damage diagnostics. *Journal of Intelligent Material Systems and Structures* 2004; **15**:729–736.
22. Lemistre MB, Balageas DL. A hybrid electromagnetic acousto-ultrasonic method for SHM of carbon/epoxy structures. *Structural Health Monitoring: An International Journal* 2003; **2**:153–160.
23. Giurgiutiu V. *Structural Health Monitoring with Piezoelectric Wafer Active Sensors*. Elsevier Academic Press: Boston, 2008.
24. Wilcox PD. Omni-directional guided wave transducer arrays for the rapid inspection of large areas of plate structures. *IEEE Transactions on Ultrasonics, Ferroelectrics, and Frequency Control* 2003; **50**:699–709.
25. Yu L, Giurgiutiu V. Multi-mode damage detection methods with piezoelectric wafer active sensors. *Journal of Intelligent Material Systems and Structures* 2009; **20**:1329–1341.
26. Ostachowicz W, Kudela P, Malinowski P, Wandowski T. Damage localisation in plate-like structures based on PZT sensors. *Mechanical Systems and Signal Processing* 2009; **23**:1805–1829.
27. Yan F, Royer Jr. RL, Rose JL. Ultrasonic guided wave imaging techniques in structural health monitoring. *Journal of Intelligent Material Systems and Structures* 2010; **21**:377–384.
28. Raghavan A, Cesnik CES. Finite-dimensional piezoelectric transducer modeling for guided wave based structural health monitoring. *Smart Materials and Structures* 2005; **14**:1448–1461.
29. Inman DJ, Farrar CR, Lopes Jr. V, Steffen Jr. V. *Damage Prognosis: For Aerospace, Civil and Mechanical Systems*. John Wiley & Sons, Inc.: Chichester, (2005).
30. Lu Y, Ye L, Su Z, Yang C. Quantitative assessment of through-thickness crack size based on Lamb wave scattering in aluminium plates. *NDT&E International* 2008; **41**(1):59–68.
31. Zhou C, Su Z, Cheng L. Quantitative evaluation of orientation-specific damage using elastic waves and probability-based diagnostic imaging. *Mechanical Systems and Signal Processing* 2011; DOI: 10.1016/j.ymssp.2011.02.001.